

Band Meandering due to Charged Impurity Effects and Carrier Transport in Ternary Topological Insulators

Kanav Sharma,¹ Niranjay K R,¹ Radha Krishna Gopal,² and Chiranjib Mitra¹

¹*Department of Physical Sciences, Indian Institute of Science Education and Research Kolkata, Nadia, 741246, West Bengal, India*

²*Department of Physics and Material Sciences and Engineering, Jaypee Institute of Information Technology, Sector 62, Noida, India*

(*Electronic mail: chiranjib@iiserkol.ac.in)

(Dated: 14 July 2025)

In this study, we investigated the impact of charged impurities on the electrical properties of the topological insulator $(\text{Bi}_{0.3}\text{Sb}_{0.7})_2\text{Te}_3$ (BST) and its indium-doped counterpart, $\text{In}_{0.14}(\text{Bi}_{0.3}\text{Sb}_{0.7})_{1.86}\text{Te}_3$ (IBST), using field-effect gating. For thin BST (30 nm), charged impurities, potentially from silicon dioxide substrate traps, contribute to band tail-type localization, with the impurity density ($n_{\text{imp}} = 10^{11} \text{ cm}^{-2}$) suggesting an external influence, though quantitative confirmation is needed. In contrast, thick BST (60 nm) exhibits potential fluctuations driven by inherent impurities ($n_{\text{imp}} = 2.23 \times 10^{14} \text{ cm}^{-2}$), forming electron-rich (n-type) and hole-rich (p-type) regions that cause band meandering near the chemical potential. Indium doping in thin IBST significantly increases the impurity density to $1.53 \times 10^{15} \text{ cm}^{-2}$, exacerbating these fluctuations and reducing mobility due to enhanced scattering. Gate-dependence analysis further revealed a temperature-driven transition from n-type to p-type characteristics at elevated temperatures (170 K), attributed to thermal activation of holes in p-type regions. These findings highlight the critical role of impurity management in optimizing topological insulators for applications in spintronics and quantum computing.

Topological insulators^{1–8} are unique quantum materials characterized by conducting surface states and bulk insulating states. This duality arises from the intricate interplay of their spin-momentum locking and time-reversal symmetry protection. The spin-momentum locking property ensures that the direction of an electron's spin is intrinsically tied to its momentum, leading to robust surface conduction channels that are resilient to scattering from non-magnetic impurities or defects. These features make topological insulators highly promising for transformative applications across diverse fields. In spintronics,^{9,10} their spin-momentum lock surface states enable efficient spin transport, minimizing energy loss and enhancing device performance. In quantum computing,¹¹ the topologically protected surface states hold potential for creating fault-tolerant qubits, paving the way for more stable quantum systems. Beyond these, topological insulators find applications in novel optoelectronic devices, high-speed transistors, and even in exploring a variety of physical phenomena, making

them pivotal in both applied science and fundamental research. Their unique properties continue to drive innovation, positioning them at the forefront of cutting-edge technological advancements.

Dirac materials have captivated researchers due to their exceptional properties. The linear energy dispersion of Dirac electrons allows them to behave uniquely within these materials, leading to fascinating phenomena. Efforts are concentrated on maintaining the chemical potential near the Dirac point (DP) through methods like doping or electrical gating. In pristine conditions-free from internal or external impurities—Dirac electrons exhibit remarkable mobility. However, challenges arise due to any inherent charged impurities present in the system or when oxide dielectrics introduce charged impurities emanating from substrate contributions. Keeping the chemical potential near the DP under such scenarios results in complications. Since the density of states near DP is minimal, local impurities can lead to significant potential fluctuations, causing band meandering.¹² This, in turn,

generates charge puddles within the material. Studies reveal that charge puddles causes backscattering, which severely diminishes the performance of Dirac electrons. Graphene, the most extensively studied Dirac material, demonstrates fluctuations in charge density caused by charge-donating impurities beneath the graphene sheet. Scanning tunneling microscopy and spectroscopy have been employed by researchers to analyze these effects and explore the origin of spatial charge inhomogeneity in graphene.¹³ Similarly, Yao et al. identified that using MoS_2 as a substrate results in charge density inhomogeneities in germanene, forming charge puddles near the DP.¹⁴

Charge puddle formation is also common in topological insulators (TIs), and is a prominent topic in condensed matter physics research. These puddles arise from potential fluctuations induced by material compensation or local impurities. Band edges are modulated as a result, forming regions with positive and negative charges. Skinner et al. demonstrated that low resistivity in TIs is caused by band bending, arising out of inadequately screened fluctuations in the random Coulomb potential.¹² Using numerical simulations, they observed that the bulk resistivity's activation energy is only 0.15 times the band gap. This insight highlights charge puddles' impact on TIs' electrical properties. Understanding charge puddles is essential for optimizing Dirac materials for applications in quantum devices and spintronics. Further research on charge puddles is required to uncover intricate mechanisms underlying these materials extraordinary properties and expand their technological potential.

Pulsed laser deposition (PLD)^{15,16,17} is a versatile and cost-effective technique widely utilized for the growth of polycrystalline crystals, offering an efficient approach to study the quantum properties of various materials. This method involves the use of high-energy laser pulses directed at a target material, which causes the ablation of its surface and the ejection of atoms and ions. These particles are subsequently deposited onto a substrate, forming a thin film. The key advantage of PLD lies in its ability to precisely control the stoichiometry and thickness of the deposited films, enabling the fabrication of high-quality crystals tailored for specific quantum property investigations. Furthermore, PLD is adapt-

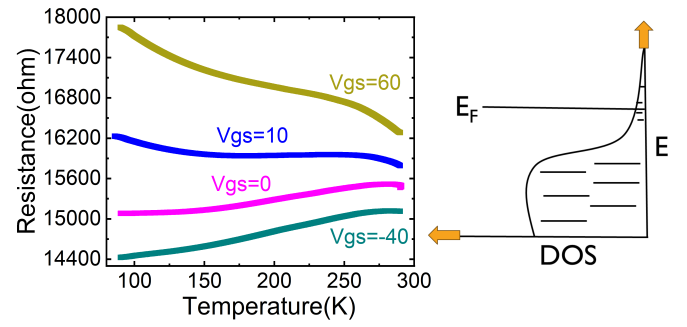


FIG. 1: Shows resistance vs temperature at different gate voltages denoted by V_{gs} in volts. The figure on the right shows density of states of the valence band versus energy with chemical potential E_F at the band tail.

able to a wide range of materials, including complex oxides, topological insulators, and superconductors, making it an invaluable tool in experimental condensed matter physics. Its flexibility allows researchers to vary deposition parameters, such as laser energy, substrate temperature, and background gas pressure, to achieve desired film characteristics. By leveraging the cost-effectiveness and precision of PLD, scientists can delve deeper into the quantum behaviors of materials, exploring phenomena like quantum Hall effects, superconductivity, and spintronics applications. We employed the same approach as before for growing our materials, utilizing the established method to ensure consistency and precision in our process.¹⁸

The chemical potential can be modified either by applying gate voltage or by doping.^{19,20,21,22,23,24} Adjusting the chemical potential provides valuable insights into material properties, particularly in small band gap materials. We have grown three materials: BST and IBST with a thickness of 30 nm, which would be referred to as thin films, and BST with a thickness of 60 nm, which would be referred to as thick films. In the 30 nm thin BST sample, the chemical potential was observed to be near the valence band tail, as depicted in Figure 1 (right) showing the density of states versus energy plot. The resistance versus temperature data at zero gate voltage indicates the metallic p-type nature of the material. When the gate voltage is increased toward positive values, Mott variable-range hopping is observed at low temperatures, where E_F shifts closer to the valence band edge. Conversely, applying negative gate voltages results in complete metal-

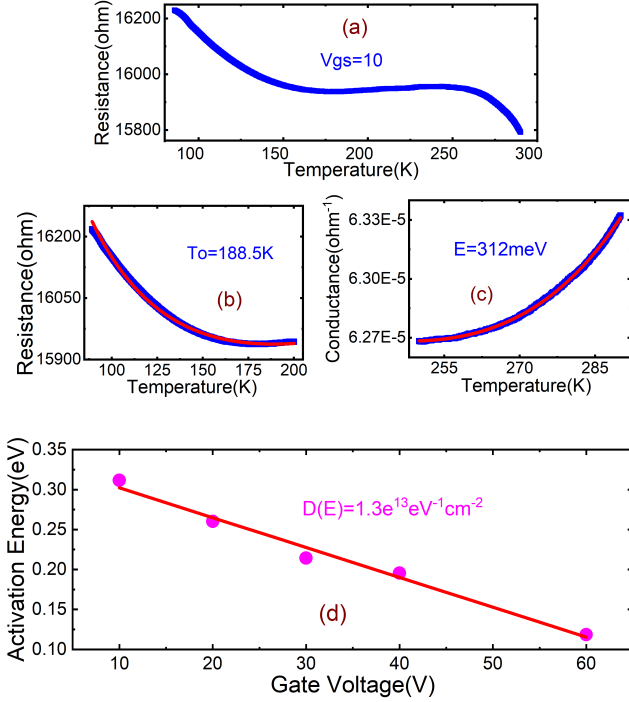


FIG. 2: (a) presents the resistance-temperature (R-T) behavior at ($V_{gs} = 10$) volts, fitted using two different approaches depicted in (b) and (c). (b) applies the Mott variable range hopping model, utilizing Equation 1 for fitting. (c) employs the parallel resistor model, based on Equation 2. (d) displays activation energies at elevated temperatures for various gate voltages, where their slopes can be utilized to determine the density of states at E_F .

lic behavior, suggesting E_f moves further into the valence band. Figure 2a illustrates the resistance-temperature behavior at a gate voltage of 10 volts, fitted at low temperatures using Mott variable-range hopping shown in figure 2(b) and is given by^{25,26}

$$R(T) = A \cdot T^{0.25} \cdot \exp\left(\left(\frac{T_o}{T}\right)^{0.25}\right) \quad (1)$$

yielding $T_o = 188.5$ K, and at high temperatures using the parallel resistor model given by^{27,28}

$$G(T) = \frac{1}{a + bT} + \frac{1}{c \exp\left(\frac{E}{k_b T}\right)} \quad (2)$$

providing an activation energy of 312 meV.

The insulating behavior observed at elevated temperatures across all positive gate voltages allows for the calculation of activation energy. At $V_{gs} = 10$ volts, this calculation is demonstrated in figure 2(c) using the parallel resistor model. For positive gate voltages, activation energies were determined and

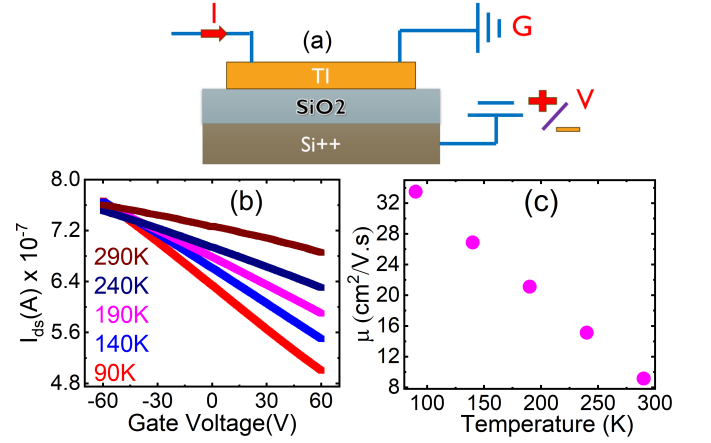


FIG. 3: (a) illustrates a thin film of topological insulator placed on a Si/SiO2 substrate, with a positive or negative gate voltage (+/- V) applied to the Si++ wafer. The current through the topological insulator is denoted as I , and G represents the common ground. (b) depicts the relationship between drain-source current and gate voltage at various temperatures. (c) presents the field-effect mobility as a function of temperature, derived using Equation 3.

subsequently plotted against gate voltages in figure 2(d). The slope of this plot facilitated the estimation of the density of states at the chemical potential. Using quantum capacitance formulations given by,²⁹

$$\frac{dE_F}{dV_g} = -\frac{dE_a}{dV_g} = \frac{eC_{ox}}{C_{ox} + C_d} \quad (3)$$

where $C_d = e^2 D(E)$ and C_{ox} is the oxide capacitance per unit area. The density of states $D(E)$ at the chemical potential was extracted which came out to be $1.3 \times 10^{13} \text{ eV}^{-1} \text{ cm}^{-2}$.

We have also calculated the four-probe mobility given by,³⁰

$$\mu = \left(\frac{L}{WC_{ox} V_{ds}}\right) \cdot \frac{\partial I_{ds}}{\partial V_{gs}} \quad (4)$$

Figure 3(a) illustrates the specific device used for gating, featuring a 300 nm thick SiO2 layer. At different temperatures, the drain-source current converges at -60 V, indicating that a negative voltage shifts the chemical potential towards the valence band, as depicted in Figure 3b. Figure 3c demonstrates that the mobility increases with decreasing temperature, which is attributed to the dominance of surface states at lower temperatures. This observed order of mobility is consistent with recent findings based on Hall measurements.³¹ However,

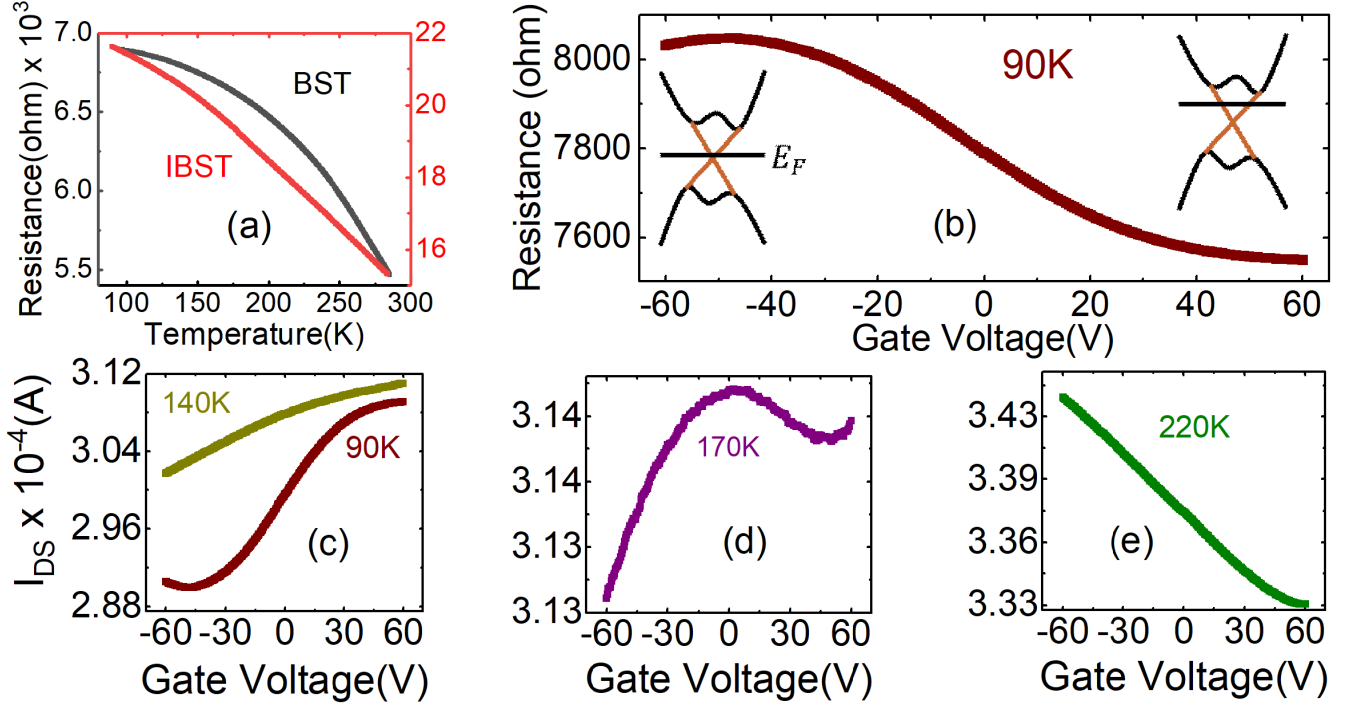


FIG. 4: (a) Shows R-T of thick-BST and thin-IBST. (b) The R-V_{gs} plot demonstrates a peak in resistance, corresponding to the charge neutrality point for BST. (c,d,e) depicts the relationship between drain-source current and gate voltage at various temperatures for BST.

the mobility values remain relatively low, likely due to the polycrystalline nature of the PLD-grown samples, which include grain boundaries and exhibit a more disordered structure, influencing the observed behavior. Using Drude's model, $\sigma = ne\mu$ at 90K with the approximation of surface conduction we calculated intrinsic carrier concentration n to be $2 \times 10^{13} \text{cm}^{-2}$. This value is large enough to say that the chemical potential is at the tail of valence band. Further we have calculated charged impurity density n_{imp} around 90K from D(E) using thermal energy $K_B * T$ gives $n_{imp} = 10^{11} \text{cm}^{-2}$. This impurity density could be the effect of oxide traps of silicon dioxide as it does not matches with the intrinsic doping value n .^{32,33} However, no quantitative estimate is available to prove this possibility.

The temperature dependence of resistance for thick BST and thin IBST is shown in Figure 4(a). The activation energies for BST and IBST, calculated using Equation 2, are 114 meV and 65.7 meV, respectively. The insulating behavior indicates that the chemical potential lies within the band gap, where the density of states is low, and local impurities may cause potential fluctuations. In the case of

BST, at 90K, the peak in resistance as a function of gate voltage appears to be approximately -55 Volts, as shown in Figure 4(b). This resistance peak spans a broad range of gate voltage, likely due to CNP smearing within our material. The inset schematic provides a depiction of the chemical potential's position inside the band. At CNP, the intrinsic doping is defined as¹⁹:

$$n = \frac{C_{ox} V_{CNP}}{e} \quad (5)$$

The calculated value of n is $3.95 \times 10^{12} \text{cm}^{-2}$ which is an order of magnitude lesser than the previous case as now the chemical potential is inside the band gap and is consistent with previous reports in similar TI thin films³⁴. Using equation 1a of kim et al.³⁵ we calculated the n_{imp} . The value came out to be $2.23 \times 10^{14} \text{cm}^{-2}$ using constant $C = 30$. This large value of n_{imp} shows that the charged impurities are inherent to the material.³⁶ Using,³⁵

$$\mu_{FE} = \frac{C \cdot e}{n_{imp} \cdot h} \quad (6)$$

and the above value of n_{imp} we calculated the field effect mobility which came out to be $32.5 \text{cm}^2/\text{V.s.}$

This value is close to what we calculated using equation 4 at 90K shown in figure 5(a). This shows $C = 30$ is a reasonable value to be used here. Figure 4(c) presents the drain-source current versus gate voltage, showcasing the material's n-type behavior at low temperatures. However, at an intermediate temperature of approximately 170K, an unusual transition occurs shown in figure 4(d). At elevated temperatures, the material shifts to a p-type characteristic shown in figure 4(e).^{37,38} This is due to p-n regions formed near the chemical potential. These p-n regions arise from potential fluctuations induced by charged impurities, either inherent to the material or introduced by oxide traps in the SiO₂ substrate. At low temperatures, the chemical potential's proximity to the conduction band favors electron-dominated (n-type) conduction, primarily through surface states. As temperature increases to 170 K and beyond, thermal energy activates holes from the valence band, enhancing the contribution of hole-rich (p-type) regions formed by band meandering. To delve deeper into this phenomenon, we examined mobility not only in BST but also in its indium-doped variation, IBST, which causes a further shift in the chemical potential of the thin film. In thin IBST, the charged impurity density n_{imp} reaches $1.53 \times 10^{15} \text{ cm}^{-2}$, an order of magnitude higher than in BST, indicating that these impurities are intrinsic to the sample and significantly enhanced by indium doping. This increase in impurity density intensifies potential fluctuations, leading to pronounced band meandering and the formation of p-n regions near the chemical potential, as discussed earlier. These regions, consisting of localized electron-rich (n-type) and hole-rich (p-type) charge puddles, enhance scattering of surface electrons, resulting in a concomitant decrease in field-effect mobility, as observed in Figure 5(b). Specifically, the mobility in IBST drops significantly compared to BST, reflecting the dominant role of impurity-induced scattering in disrupting the topologically protected surface conduction. This behavior underscores the challenge of maintaining high mobility in doped topological insulators and suggests that controlling impurity levels is critical for optimizing their performance in applications such as spintronics and quantum computing.

In conclusion, our findings demonstrate that

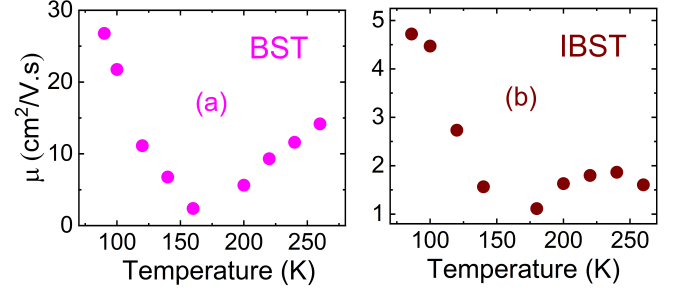


FIG. 5: (a) illustrates the four-probe field-effect mobility for 60nm BST. (b) demonstrates that after doping with indium, the magnitude of mobility decreases while maintaining the same temperature-dependent behavior.

charged impurities, including those likely arising from silicon dioxide traps, significantly influence the electronic band structure of ternary topological insulators, leading to the formation of band tails in both the conduction and valence bands. The observed charge neutrality point (CNP) within the band gap, as seen in thick BST and thin IBST, indicates that when the chemical potential resides near the CNP, these impurities induce potential fluctuations, causing band meandering and the formation of localized electron-rich (n-type) and hole-rich (p-type) charge puddles. This band meandering drives a transition from n-type to p-type characteristics at elevated temperatures (170 K and above), as thermal energy enhances hole activation in p-type regions, as evidenced in Figure 4(b). While the impurity density in thin BST ($n_{\text{imp}} = 10^{11} \text{ cm}^{-2}$) suggests a contribution from SiO₂ oxide traps, as it deviates from the intrinsic doping level, further quantitative studies are needed to confirm their precise role. Intentional indium doping in IBST exacerbates these effects, increasing the charged impurity density to $1.53 \times 10^{15} \text{ cm}^{-2}$, which intensifies scattering of surface electrons and reduces field-effect mobility, as shown in Figure 5(b). These results underscore the critical impact of impurities on the performance of topological insulators and highlight the need for strategies to control both substrate-related and intrinsic impurities to optimize their topologically protected surface states for applications in spintronics and quantum computing.

The authors acknowledge the University Grant Commission (UGC) of the Government of India for

financial support.

AUTHOR DECLARATIONS

Conflict of Interest

The authors have no conflicts to disclose.

Author Contributions

Kanav Sharma: Conceptualization (lead); Formal analysis (lead); Data curation (lead); Investigation (lead); Writing – original draft (lead); **Niranjay K R:** Data curation (supporting); Software (supporting); **Radha Krishna Gopal:** Review & editing (supporting). **Chiranjib Mitra:** Formal analysis (equal); Supervision (lead); Writing – review & editing (equal).

DATA AVAILABILITY

The data that support the findings of this study are available from the corresponding author upon reasonable request.

REFERENCES

- ¹M. Z. Hasan and C. L. Kane, “Colloquium: Topological insulators,” *Rev. Mod. Phys.* **82**, 3045–3067 (2010).
- ²C. L. Kane and E. J. Mele, “Topological order and the quantum spin hall effect,” *Physical Review Letters* **95** (2005), 10.1103/physrevlett.95.146802.
- ³X.-L. Qi and S.-C. Zhang, “Topological insulators and superconductors,” *Reviews of modern physics* **83**, 1057 (2011).
- ⁴Y. Tokura, K. Yasuda, and A. Tsukazaki, “Magnetic topological insulators,” *Nature Reviews Physics* **1**, 126–143 (2019).
- ⁵J. E. Moore, “The birth of topological insulators,” *Nature* **464**, 194–198 (2010).
- ⁶R. Shankar, “Topological insulators—a review,” *arXiv preprint arXiv:1804.06471* (2018).
- ⁷B. A. Bernevig, T. L. Hughes, and S.-C. Zhang, “Quantum spin hall effect and topological phase transition in hgte quantum wells,” *science* **314**, 1757–1761 (2006).
- ⁸L. Fu, C. L. Kane, and E. J. Mele, “Topological insulators in three dimensions,” *Physical review letters* **98**, 106803 (2007).
- ⁹Y. Fan and K. L. Wang, “Spintronics based on topological insulators,” in *Spin*, Vol. 6 (World Scientific, 2016) p. 1640001.
- ¹⁰S. Pal, A. Nandi, S. G. Nath, P. K. Pal, K. Sharma, S. Manna, A. Barman, and C. Mitra, “Enhancement of spin to charge conversion efficiency at the topological surface state by inserting normal metal spacer layer in the topological insulator based heterostructure,” *Applied Physics Letters* **124** (2024).
- ¹¹L. Fu and C. L. Kane, “Superconducting proximity effect and majorana fermions at the surface of a topological insulator,” *Physical review letters* **100**, 096407 (2008).
- ¹²B. Skinner, T. Chen, and B. I. Shklovskii, “Why is the bulk resistivity of topological insulators so small?” *Phys. Rev. Lett.* **109**, 176801 (2012).
- ¹³Y. Zhang, V. W. Brar, C. Girit, A. Zettl, and M. F. Crommie, “Origin of spatial charge inhomogeneity in graphene,” *Nature Physics* **5**, 722–726 (2009).
- ¹⁴Q. Yao, Z. Jiao, P. Bampoulis, L. Zhang, A. Rudenko, M. Katsnelson, and H. Zandvliet, “Charge puddles in germanene,” *Applied Physics Letters* **114** (2019).
- ¹⁵A. Pandey, S. Singh, B. Ghosh, S. Manna, R. Gopal, and C. Mitra, “Pulsed laser deposition of highly c-axis oriented thin films of bsts topological insulator,” (2019), *arXiv:1910.08100 [cond-mat.mtrl-sci]*.
- ¹⁶S. Singh, R. Gopal, J. Sarkar, A. Pandey, B. G. Patel, and C. Mitra, “Linear magnetoresistance and surface to bulk coupling in topological insulator thin films,” *Journal of Physics: Condensed Matter* **29**, 505601 (2017).
- ¹⁷C. Mitra, G. Köbernik, K. Dörr, K.-H. Müller, L. Schultz, P. Raychaudhuri, R. Pinto, and E. Wieser, “Magnetotransport properties of a room temperature rectifying tunnel junction made of electron and hole doped manganites,” *Journal of applied physics* **91**, 7715–7717 (2002).
- ¹⁸K. Sharma, R. Banerjee, A. Nandi, R. K. Gopal, and C. Mitra, “Suppression of generation-recombination noise in topological insulators through indium substitution,” *arXiv preprint arXiv:2410.06291* (2024).
- ¹⁹S. Bhattacharyya, M. Banerjee, H. Nhalil, S. Islam, C. Dasgupta, S. Elizabeth, and A. Ghosh, “Bulk-induced 1/f noise at the surface of three-dimensional topological insulators,” *ACS nano* **9**, 12529–12536 (2015).
- ²⁰Y. Xu, I. Miotkowski, and Y. P. Chen, “Quantum transport of two-species dirac fermions in dual-gated three-dimensional topological insulators,” *Nature communications* **7**, 11434 (2016).
- ²¹A. Taskin, H. F. Legg, F. Yang, S. Sasaki, Y. Kanai, K. Matsumoto, A. Rosch, and Y. Ando, “Planar hall effect from the surface of topological insulators,” *Nature communications* **8**, 1340 (2017).
- ²²R. Zhong, J. Schneeloch, Q. Li, W. Ku, J. Tranquada, and G. Gu, “Indium substitution effect on the topological crystalline insulator family (pb1-x sn x) 1-y in y te: Topological and superconducting properties,” *Crystals* **7**, 55 (2017).
- ²³G. Du, Z. Du, D. Fang, H. Yang, R. Zhong, J. Schneeloch, G. Gu, and H.-H. Wen, “Fully gapped superconductivity in in-doped topological crystalline insulator pb 0.5 sn 0.5 te,” *Physical Review B* **92**, 020512 (2015).
- ²⁴M. Brahlek, N. Bansal, N. Koirala, S.-Y. Xu, M. Neupane, C. Liu, M. Z. Hasan, and S. Oh, “Topological-metal to band-insulator transition in (bi 1-x in x) 2 se 3 thin films,” *Physical review letters* **109**, 186403 (2012).
- ²⁵K. Lisunov, M. Guc, S. Levchenko, D. Dumcenco, Y.-S. Huang, G. Gurieva, S. Schorr, and E. Arushanov, “Energy spectrum of near-edge holes and conduction mechanisms in cu2znse4 single crystals,” *Journal of alloys and compounds* **580**, 481–486 (2013).
- ²⁶N. F. Mott and E. A. Davis, *Electronic processes in non-crystalline materials* (OUP Oxford, 2012).
- ²⁷S. Singh, R. Gopal, J. Sarkar, A. Pandey, B. G. Patel, and C. Mitra, “Linear magnetoresistance and surface to bulk coupling in topological insulator thin films,” *Journal of Physics: Condensed Matter* **29**, 505601 (2017).
- ²⁸C. Mitra, P. Raychaudhuri, J. John, S. Dhar, A. Nigam, and R. Pinto, “Growth of epitaxial and polycrystalline thin films of the electron doped system la 1-x ce x mno 3 through pulsed laser deposition,” *Journal of Applied Physics* **89**, 524–530 (2001).
- ²⁹J. Xue, S. Huang, J.-Y. Wang, and H. Xu, “Mott variable-range hopping transport in a mos 2 nanoflake,” *RSC advances* **9**, 17885–17890 (2019).
- ³⁰S. Ghatak, A. N. Pal, and A. Ghosh, “Nature of electronic states in atomically thin mos2 field-effect transistors,” *ACS nano* **5**, 7707–7712 (2011).
- ³¹R. K. Gopal, S. Singh, R. Chandra, and C. Mitra, “Weak-antilocalization and surface dominated transport in topological insulator bi2se2te,” *AIP Advances* **5** (2015).
- ³²K. M. Burson, W. G. Cullen, S. Adam, C. R. Dean, K. Watanabe, T. Taniguchi, P. Kim, and M. S. Fuhrer, “Direct imaging of charged impurity density in common graphene substrates,” *Nano letters* **13**, 3576–3580 (2013).
- ³³A. Deshpande, W. Bao, F. Miao, C. N. Lau, and B. J. LeRoy, “Spatially resolved spectroscopy of monolayer graphene on sio2,” *Phys. Rev. B* **79**, 205411 (2009).
- ³⁴I. T. Rosen, I. Yudhistira, G. Sharma, M. Salehi, M. A. Kastner, S. Oh, S. Adam, and D. Goldhaber-Gordon, “Absence of strong localization at low conductivity in the topological surface state of low-disorder sb2te3,” *Phys. Rev. B* **99**, 211101 (2019).
- ³⁵D. Kim, S. Cho, N. P. Butch, P. Syers, K. Kirshenbaum, S. Adam, J. Paglione, and M. S. Fuhrer, “Surface conduction of topological dirac electrons in bulk insulating bi2se3,” *Nature Physics* **8**, 459–463 (2012).
- ³⁶S. Islam, S. Bhattacharyya, A. Kandala, A. Richardella, N. Samarth, and A. Ghosh, “Bulk-impurity induced noise in large-area epitaxial thin films of topological insulators,” *Applied Physics Letters* **111** (2017).
- ³⁷Z. Ren, A. A. Taskin, S. Sasaki, K. Segawa, and Y. Ando, “Large bulk resistivity and surface quantum oscillations in the topological insulator bi2te2se,” *Phys. Rev. B* **82**, 241306 (2010).
- ³⁸A. A. Taskin, Z. Ren, S. Sasaki, K. Segawa, and Y. Ando, “Observation of dirac holes and electrons in a topological insulator,” *Phys. Rev. Lett.* **107**, 016801 (2011).